ACS NANO

www.acsnano.org

ARTICLE

3D Crumpled Ultrathin 1T MoS_2 for Inkjet Printing of Mg-Ion Asymmetric Micro-supercapacitors

Yuanlong Shao,* Jui-Han Fu, Zhen Cao, Kepeng Song, Ruofan Sun, Yi Wan, Atif Shamim, Luigi Cavallo, Yu Han, Richard B. Kaner,* and Vincent C. Tung*

Cite This: *ACS Nano* 2020, 14, 7308–7318

Read Online

ACCESS | Metrics & More | Article Recommendations | Supporting Information

ABSTRACT: **Metallic molybdenum disulfide (MoS_2), *e.g.*, 1T phase, is touted as a highly promising material for energy storage that already displays a great capacitive performance. However, due to its tendency to aggregate and restack, it remains a formidable challenge to assemble a high-performance electrode without scrambling the intrinsic structure. Here, we report an electrohydrodynamic-assisted fabrication of 3D crumpled MoS_2 (c-MoS_2) and its formation of an additive-free stable ink for scalable inkjet printing. The 3D c-MoS_2 powders exhibited a high concentration of metallic 1T phase and an ultrathin structure. The aggregation-resistant properties of the 3D crumpled particles endow the electrodes with open space for electrolyte ion transport. Importantly, we experimentally discovered and theoretically validated that 3D 1T c-MoS_2 enables an extended electrochemical stable working potential range and enhanced capacitive performance in a bivalent magnesium-ion aqueous electrolyte. With reduced graphene oxide (rGO) as the positive electrode material, we inkjet-printed 96 rigid asymmetric micro-supercapacitors (AMSCs) on a 4-in. Si/SiO_2 wafer and 100 flexible AMSCs on photo paper. These AMSCs exhibited a wide stable working voltage of 1.75 V and excellent capacitance retention of 96% over 20 000 cycles for a single device. Our work highlights the promise of 3D layered materials as well-dispersed functional materials for large-scale printed flexible energy storage devices.**

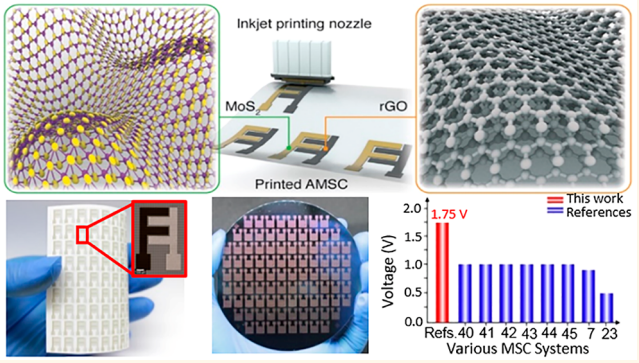

KEYWORDS: *supercapacitors, MoS_2, printing technique, Mg-ion, microdevice*

Recent advancements in portable electronics and emerging interest in wearable miniaturized devices, on-body medical monitors, and the Internet of Things (IoT) nodes have propelled the needs for miniaturized portable energy storage devices.[1−4] To enable direct integration with functional electronic/sensing units at scale, small-size and discrete energy storage devices need to be reasonably thin, mechanically robust, electrochemically durable, and dynamically flexible in nature. However, feasible designs in device architecture and viable manufacturing means of fabricating miniaturized energy storage components, such as micro-supercapacitors (MSCs), for energy delivery or harvesting with high power and energy capabilities remain a significant challenge.[5,6] An array of cost-effective manufacturing processes for MSCs needs to address the pressing needs. Notable innovations of fabricating MSCs include laser scribing/ablation,[7,8] electrochemical deposition,[9] vacuum filtration,[10,11] and spray-coating.[12] These pioneering demonstrations, while promising, cannot precisely "print out" elaborated designs of micropatterns with high resolution and excellent reliability, especially when more than one type of active material needs to be deposited, which is a key prerequisite for expanded stable electrochemical potential windows through the deployment of asymmetric MSCs (AMSCs).[13] Meanwhile, inkjet printing offers a promising contactless deposition strategy to create complex layouts of multifunctional materials with well-defined features and

Received: March 26, 2020
Accepted: June 1, 2020
Published: June 1, 2020

https://dx.doi.org/10.1021/acsnano.0c02585
ACS Nano 2020, 14, 7308–7318

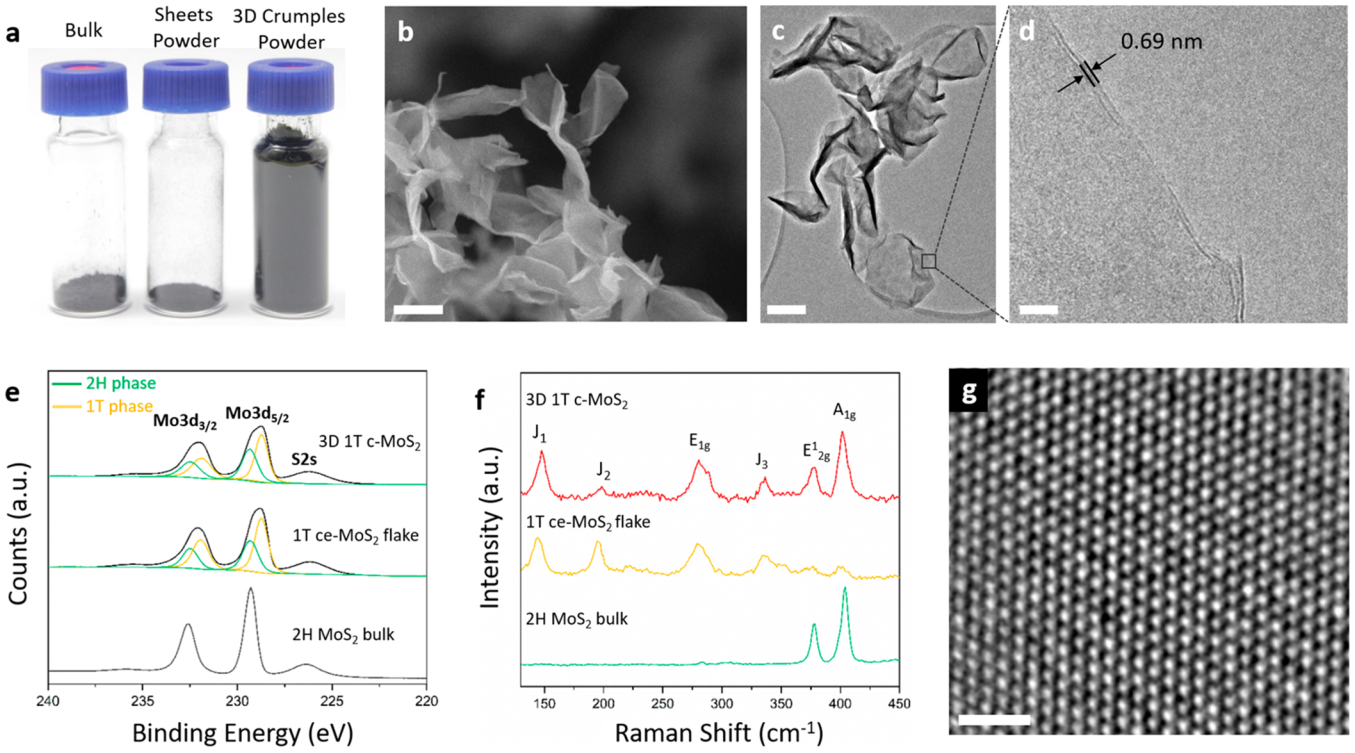

Figure 1. Preparation and characterization of a 3D c-MoS_2 dispersion with a high concentration of 1T phase. (a) Photograph featuring the transition from (left) bulk MoS_2 powder, (middle) ce-MoS_2 sheets, and (right) the solid 3D 1T c-MoS_2 powder in vials with the same weight for comparison. It is apparent that crumpling of planar 1T ce-MoS_2 sheets into 3D 1T c-MoS_2 results in a significant volumetric expansion. (b) SEM image shows the morphology of as-printed 3D 1T c-MoS_2. Scale bar: 200 nm. (c) Low-magnification TEM image of a single 3D 1T c-MoS_2. Scale bar: 200 nm. (d) Magnified TEM image of a 3D 1T c-MoS_2 edge. (e, f) Representative high-resolution XPS spectra of the Mo 3d peaks and Raman spectra for 3D 1T c-MoS_2, ce-1T MoS_2 flake, and 2H MoS_2 bulk, respectively. (g) HRTEM analysis reveals the preservation of the octahedral arrangement of the 3D 1T c-MoS_2.

morphologies, over a myriad of substrates in a high-throughput fashion.[14−18]

Inkjet printing can provide an attractive route to low-cost fabrication of MSCs with multifunctional active materials and high resolution. The new class of two-dimensional materials, including graphene,[19−21] transition-metal dichalcogenides (TMDs),[14,16] and MXenes,[22,23] shows great promise for use in inkjet-printed flexible electronics, because their atomic thickness allows for maximum active surface area, unique electronic properties, and mechanical flexibility. As a promising TMD for energy storage devices,[24−26] 1T metallic molybdenum disulfide (MoS_2) has been investigated extensively due to its unique layered structure, good electrochemical performance, and the earth abundance of bulk MoS_2 as a mineral.[27−29] Typically, the 1T phase exhibits significantly enhanced hydrophilicity and an electrical conductivity at least 5 orders of magnitude higher than that of 2H-MoS_2, which result in an extreme high volumetric capacitance of ~700 F cm^{-3} in an aqueous electrolyte.[24] Thus, 1T MoS_2 could be an ideal material to fabricate high-performance MSCs. However, just like other typical 2D materials, layered MoS_2 sheets tend to restack through out-of-plane van der Waals interactions, which not only decreases the active surface area but also hinders efficient electrolyte ion diffusion, resulting in a rapid decay of electrochemical performance. Converting the ultrathin 2D materials to 3D atomic thick building blocks without sacrificing the intrinsic atomic thickness for inkjet printing, MSCs can be a promising strategy to solve the restacking issue.

Here, we report an electrohydrodynamic-assisted method (electrospray) to prepare a 1T phase dominated by 3D crumpled MoS_2 (c-MoS_2) as a powder and its stable ink formation for inkjet printing of MSCs with fine resolution. By using a volatile solvent for the MoS_2 dispersion and multijetting mode, the extremely fast solvent evaporation and ink solidification of the electrospray process guarantee a high proportion of the 1T phase and an ultrathin structure of the obtained 3D c-MoS_2 powder. After dispersion in an optimized mixed binary alcohol solvent, MoS_2 ink is prepared without introducing any obvious phase transformation of the 1T MoS_2 often caused by temperature variation or chemical treatment. AMSCs made of 3D 1T c-MoS_2 inks and reduced graphene oxide (rGO) wrinkled flakes can be precisely printed onto large substrates with an interdigitated pattern. The inkjet printing of 96 AMSCs on a 4 in. Si/SiO_2 wafer and 100 flexible AMSCs on a 10 cm × 10 cm EPSON photopaper demonstrates the scalability and high resolution of the inkjet printing technique. A single printed AMSC can deliver a wide stable working voltage of 1.75 V and excellent capacitance retention of 96% over 20 000 cycles, an areal energy density of 3.85 μWh cm^{-2}, and a maximum power density of 12.6 mW cm^{-2} in a Mg-ion aqueous electrolyte.

RESULTS AND DISCUSSION

Three-dimensional 1T c-MoS_2 powders were obtained through the electrospray of chemically exfoliated (ce-) MoS_2 flakes, which were synthesized by a modified Li-intercalation process.[30] Based on the photograph (Supplementary Figure

https://dx.doi.org/10.1021/acsnano.0c02585
ACS Nano 2020, 14, 7308−7318

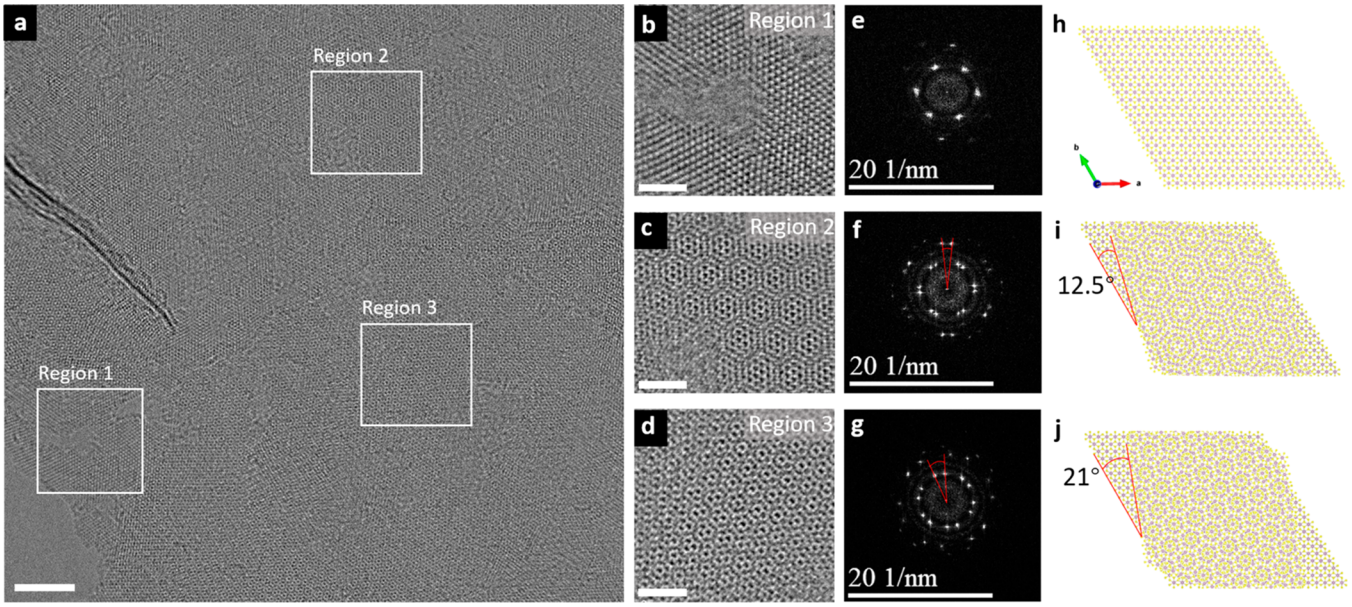

Figure 2. HRTEM characterization and fast Fourier transform (FFT) patterns of 3D c-MoS_2. (a) HRTEM image of 3D 1T c-MoS_2 containing mostly mono- (region 1) to bilayer (regions 2 and 3) MoS_2 sheets. The octahedral arrangement of the Mo atoms in region 1, corresponding to the 1T phase, is clearly shown in the (b) selected close-up view of region 1, (e) the FFT pattern, and (h) single-layer MoS_2 in the atomic model. Meanwhile, the bilayer regions exhibit two sets of twist angles (12.5° vs 21°) and the formation of two distinctive moiré patterns as confirmed by the (c, d) close-up views and (f, g) FFT patterns along with (i, j) computer-generated atomic models.

S1a inset) taken under red laser irradiation, the ce-MoS_2 flakes dispersed in isopropyl alcohol (IPA), a low-viscosity solvent, were ejected simultaneously from all directions of the capillary circumference and formed into a multiple cone with distinct streams of mist, known as multijet mode.[31] With the intense electrical shear stress at high applied electric field (1.35 kV/cm) and highly divergent jetting under the multijet mode, the size of the droplet generated can be nearly monodisperse and much smaller than that produced from single cone jet or Tayler cone jet mode.[32] The detailed electrospray deposition process of 3D 1T c-MoS_2 from a ce-MoS_2 dispersion is illustrated in the schematic in Supplementary Figure S1b and explained in Supplementary Note 1. Upon solvent evaporation-induced volumetric shrinkage, the charge density residing on the surface of the charged droplets drastically increases. After exceeding the Rayleigh limit,[33] droplets fission into numerous smaller ones, which only contain single MoS_2 flakes. The charged droplet fission is beneficial to form ultrafine and monodisperse nanoparticles, thus avoiding the aggregation of the 2D nanoflakes. Due to the continuous evaporation of solvent, the droplets keep shrinking and even start to solidify, which results in the crumpling of the MoS_2 flakes. The photograph in Figure 1a features a density comparison of bulk MoS_2, ce-MoS_2 flakes, and 3D 1T c-MoS_2 powders in glass vials with the same weight (4 mg), which demonstrates the significant volume expansion after the electrohydrodynamic-assisted fabrication process. The scanning electron microscope (SEM) and transmission electron microscope (TEM) images of the as-deposited flakes (Figure 1b,c) reveal the uniform dispersed and hierarchically porous yet thin folded walls. The high-resolution TEM (HRTEM) observation in Figure 1d demonstrates the bilayer thickness of 3D 1T c-MoS_2. The high electric field induced multijet mode is one of the crucial parameters to achieve the highly crumpled and monodispersed MoS_2. Supplementary Figure S2 demonstrates that the MoS_2 flakes significantly begin to stack and aggregate when the applied electric field voltage is decreased.

As exhibited in Figure 1e,f, X-ray photoelectron spectroscopy (XPS) and Raman spectroscopy were used to characterize the chemical states of the as-prepared 3D c-MoS_2. Deconvolution of the Mo 3d region of the 3D 1T c-MoS_2 indicates that the 1T phase ratio is 62.7%, an only minor decrease from the 64.6% of the ce-MoS_2 precursors. Following the same trend as XPS, the Raman spectra of the 3D 1T c-MoS_2 also exhibit characteristic peaks mainly to the 1T phase, including typical peaks of J_1, J_2, and J_3 modes at 221, 281, and 330 cm^{-1} and in tandem with 377 and 402 cm^{-1} assigned to the E^1_{2g} and A_{1g} modes of 2H phase. A strong Raman band at 148 cm^{-1} of 3D 1T c-MoS_2 can be attributed to the Mo−Mo stretching vibrations in 1T MoS_2. The other signature Raman shifts of c-MoS_2 at ~221, 281, and 330 cm^{-1} are also associated with the phonon modes in 1T MoS_2, which matches well with the ce-MoS_2 flake. The high 1T phase concentration was also verified by HRTEM, as shown in Figure 1g. The stacking sequence for 3D 1T c-MoS_2 follows AbC stacking, where the S atoms in the upper and lower planes are offset from each other and the Mo atoms occupy the octahedral holes of the S layer. Due to the stark contrast in atomic numbers, signals derived from S atoms in the monolayered 1T MoS_2 are relatively weak compared to the Mo atoms. Thus, the 3D 1T c-MoS_2 exhibits a hexagonal lattice signature, as can be seen in Figure 1g and Supplementary Figure S4d.

Figure 2a shows the HRTEM of the edge of a single 3D 1T c-MoS_2. Indeed, the edges of 3D 1T c-MoS_2 are mostly monolayer (Figure 2b, region 1) and exhibit a single set of 6-fold symmetry spots from the fast Fourier transform (FFT) pattern (Figure 2e), corroborating the representative hexagonal atomic structure of single-layer 1T MoS_2 (Figure 2h). Meanwhile, as suggested in Figure 2c,d, HRTEM images of region 2 and region 3 comprise two different moiré patterns with different periodicities and misorientations. Moiré patterns

https://dx.doi.org/10.1021/acsnano.0c02585
ACS Nano 2020, 14, 7308−7318

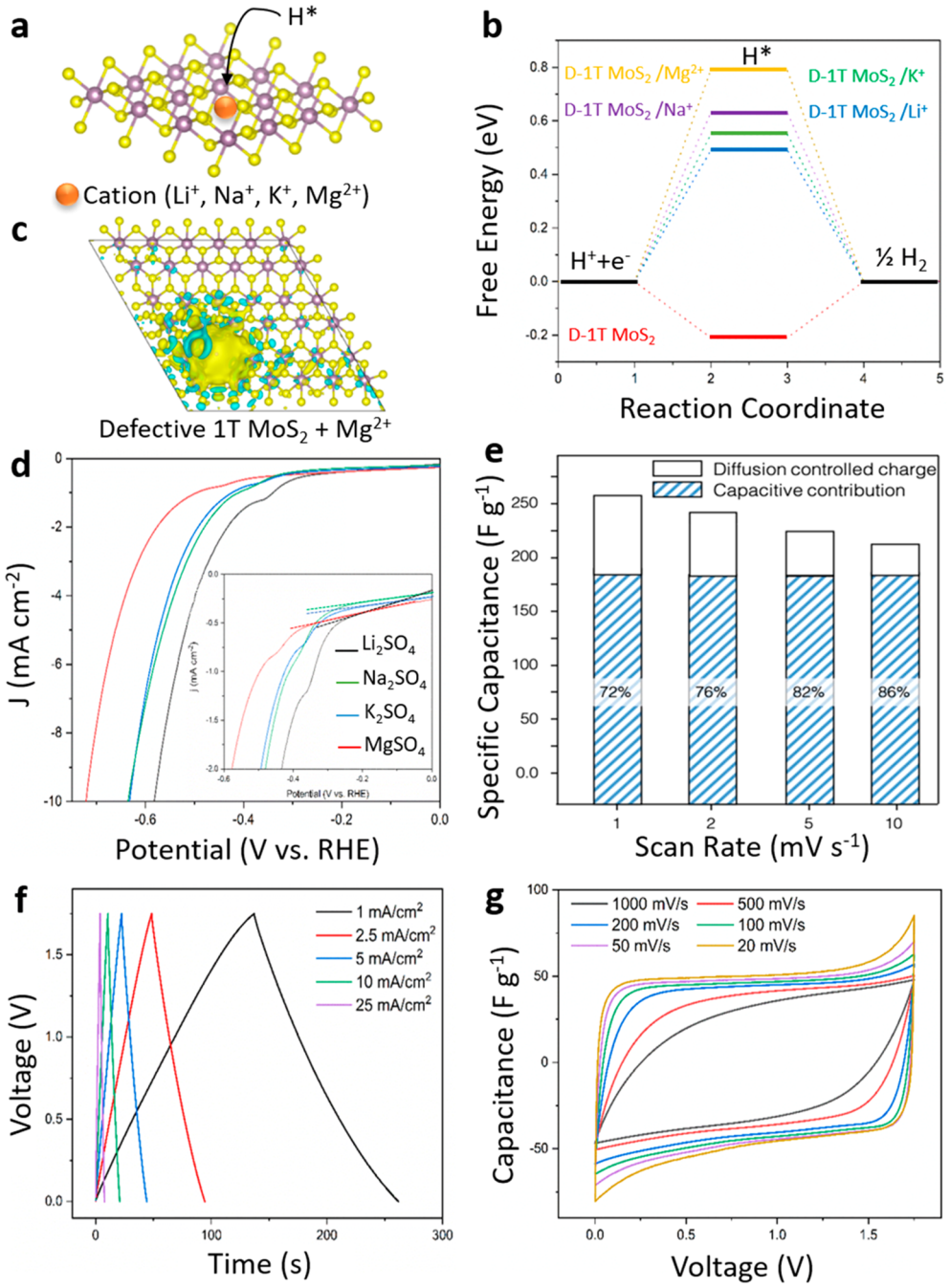

Figure 3. Theoretical insights and electrochemical characterization of 3D 1T c-MoS_2. (a) Schematic of the perspective view of defective 1T MoS_2 where adsorption of mono- and divalent ions takes place. (b) Free energy *versus* the reaction coordinate of the HER. ΔG_H is used as a descriptor for correlating the DFT prediction with experimental measurements for the HER. (c) DFT modeling reveals a surge in local electron density around the binding sites of the divalent Mg ions. (d) LSV curves of the 3D 1T c-MoS_2 electrode measured in different neutral electrolytes, including 0.5 M Li_2SO_4, 0.5 M Na_2SO_4, 0.5 M K_2SO_4, and 1.0 M $MgSO_4$. Inset shows the onset potentials for the HER. Incorporation of divalent Mg ions gives rise to significantly increased overpotential and thus the stable potential window. (e) Capacitive and diffusion-controlled contributions of the 3D 1T c-MoS_2 electrode at different scan rates. (f, g) GCD and CV curves of a 3D 1T c-MoS_2//rGO asymmetric supercapacitor at different current densities and scan rates, representatively.

typically are taken as a hallmark of enabling the stacking between monolayer crystals with disproportionate lattices and arbitrary mutual rotation. The result is an extended periodicity that emerges from the local atomic registry as shown on the basal plane of 3D 1T c-MoS_2. The corresponding FFT patterns contain double sets of 6-fold symmetry diffraction spots (Figure 2f,g). According to the measurement of the splitting spots in the FFT patterns (Supplementary Figure S3), the moiré patterns in these two regions exhibit twist angles of 12.5° and 21°, confirmed by the FFT (Figure 2f,g) and simulated atomic models (Figure 2i,j). Moiré patterns that typically arise in bilayer stacking with small misalignment between adjacent layers are found in the 1T 3D c-MoS_2, suggesting the atomic thickness of the c-MoS_2.

In order to evaluate its electrochemical performance, 3D 1T c-MoS_2 was first filtered into a freestanding film as an

https://dx.doi.org/10.1021/acsnano.0c02585
ACS Nano 2020, 14, 7308−7318

electrode. The cross-section SEM image and photograph of the freestanding 3D 1T c-MoS_2 film are shown in Supplementary Figure S4a,b. The electrical conductivity of the 3D 1T c-MoS_2 film derived from the $I-V$ curve (Supplementary Figure S4g) is 20.8 S/cm, thus allowing the formation of reasonably thick and porous films without any binding agent. The electrochemical energy storage properties of the filtered 3D 1T c-MoS_2 films were first explored in different aqueous electrolytes, such as Li_2SO_4, Na_2SO_4, K_2SO_4, and $MgSO_4$. The resulting cyclic voltammogram (CV) profiles in $MgSO_4$ exhibit a significantly wider stable operating potential and a substantially higher specific capacitance, as indicated in Supplementary Figure S5a. Achieving a stable working potential in electrochemically active materials is a crucial factor to determine the overall working voltage of the full device, in tandem with the output energy density and power density.

For the negative electrode in aqueous electrolytes, the capacitive stable working potential range is mainly determined by the initial hydrogen evolution reaction (HER) potential, which is related to the process of initial proton adsorption onto the catalyst active sites (Figure 3a). As demonstrated in Figure 3b,c, we systematically evaluated the HER behavior of defective MoS_2 mixed with different cation electrolytes within the computational hydrogen electrode model through density functional theory (DFT) calculations.[34] We first employed DFT calculations to determine the hydrogen adsorption free energy (ΔG_H) for a series of cations (Figure 3b). Consistent with previous results,[35,36] the HER can be catalyzed at the defect sites of the MoS_2 surface with a relatively low overpotential. When additional metal cations are introduced, the adsorbed metal cations are stabilized on the active sites and ΔG_H increases significantly relative to the intrinsic 1T deformed basal plane. ΔG_H continues to increase with increasing radii of metal cations and ultimately lies around 0.8 eV when the divalent cation, Mg^{2+}, resides on the defective basal plane of 1T MoS_2. The result is a surging electronic density that gives rise to the highest overpotential or the largest stable working potential among the different adsorbed cations ($Li^+ < Na^+ < K^+ < Mg^{2+}$), as suggested in the simulation model presented in Figure 3c and Supplementary Figure S5d–f.

Drawing on DFT insights, we then performed linear sweep voltammograms (LSV). As shown in Figure 3d, polarization curves of 3D 1T c-MoS_2 electrodes measured in sulfate-based electrolytes with different metal cations collectively match well with the predicted impact of adsorbed cations on the capacitive stable working potential. The corresponding overpotential, defined as the potential required to reach current densities of -10 mA/cm^2, shows that the defective MoS_2 with Mg^{2+} increases the overpotential from -0.58 V in Li_2SO_4 to -0.72 V. Accordingly, the onset potentials for HER are -0.22, -0.26, -0.24, and -0.35 V (*vs* a reversible hydrogen electrode, RHE) for Li_2SO_4, Na_2SO_4, K_2SO_4, and $MgSO_4$, respectively (Figure 3d, inset). To further verify the impact of cations, we tested monovalent and divalent electrolytes with different anions, *e.g.*, NO_3^-. It can be seen that the overpotential order for these neutral cation electrolytes within two different types of anions is nearly the same, confirming the cation-dominated effects on the capacitive stable working potential (Supplementary Figure S5c).

The nearly rectangular nature of the CV curves of 3D 1T c-MoS_2 electrode in 1.0 M $MgSO_4$ (Supplementary Figure S5a) indicates capacitive behavior for thick films of 3D 1T c-MoS_2 electrodes. These electrodes exhibited a gravimetric capacitance of 258 F g^{-1} at a scan rate of 1 mV s^{-1} and retained ~64% of their initial capacitance when the scan rate was increased up to 100 mV s^{-1} (Supplementary Figure S7a). To elucidate the correlation between the 1T phase and the electrochemical properties, we tested MoS_2 electrodes with different ratios of 1T phase. To this end, thick films made of 3D 1T c-MoS_2 were annealed at 100 °C for 1 h under ambient conditions to decrease the concentration of the 1T phase. Deconvolution of the XPS spectra of Mo core-level electron peaks revealed a significantly reduced ratio of the 1T phase (23.2%) among an emerging 2H phase (Supplementary Figure S6b–d). The local transition in atomic arrangements from octahedral to trigonal prismatic has a profound impact on the macroscale electrochemical properties. Even mixed with conductive 1T MoS_2 flakes, the 2H phase dominated 3D c-MoS_2 still displayed a specific capacitance of only 143.3 F g^{-1} at 1 mV s^{-1}, which rapidly dropped to 31.9 F g^{-1} when increasing the scan rate to 100 mV s^{-1} (Supplementary Figure S7a). Meanwhile, we obtained a slightly improved capacitance when incorporating the 3D 1T c-MoS_2 with 1T MoS_2 flakes, giving rise to a slightly improved specific capacitance of 266 F g^{-1} at a low scan rate of 1 mV s^{-1}. However, the specific capacitance drastically decreased to 109 F g^{-1} when the scan rate was increased to 100 mV s^{-1}. Compared with the cross-section and top views of the SEM images (Supplementary Figure S4a–c for the 3D 1T c-MoS_2 film and Supplementary Figure S8 for the 3D 1T c-MoS_2/ce-1T MoS_2 mixed film), it becomes clear that the dense packing of the MoS_2 flakes and the concomitant less open pores significantly impairs the electrolyte ion transport and subsequently affects the rate performance.

In order to investigate the charge storage contribution and the electrochemical dynamic behavior of the 3D 1T c-MoS_2 electrode, CV curves tested under varied scan rates were systematically analyzed to distinguish the capacitive charge contribution from the diffusion-controlled charge contribution (Supplementary Figure S9). As shown in Figure 3e, the analysis indicates 72% capacitive charge contribution at a scan rate of 1 mV s^{-1}, which is enhanced to 86% when the scan rate is increased up to 10 mV s^{-1}. Such a high capacitive contribution even at a low scan rate could be another reason for the high rate performance of the 3D 1T c-MoS_2 electrode. In order to fully take advantage of the wide negative potential range of the 3D 1T c-MoS_2 electrode, we used reduced graphene oxide film as the positive electrode to assemble an asymmetric supercapacitor. As demonstrated in the galvanostatic charge and discharge (GCD) (Figure 3f) and CV (Figure 3g) curves, the assembled asymmetric supercapacitor can be stably charged/discharged with an output voltage of 1.75 V. The CV curve remains rectangular even when the scan rate is increased to 1000 mV s^{-1}, indicating the high-power capability and good rate performance for the asymmetric device. The great intrinsic electrochemical performance of the 3D 1T c-MoS_2 can guarantee the excellent energy storage capability of the micro-supercapacitor.

We then built MSCs using an inkjet printing technique. In order to achieve high-resolution inkjet-printed MSCs, some important criteria must be taken into account to form very stable jetting: (1) a sufficiently stable ink during jetting; (2) well-matched liquid and solid surface tension/wetting dynamics to establish a spatially uniform material deposition; and (3) particle sizes less than 1/20 that of the nozzle diameter to avoid the jetting nozzle plugging. The choice of solvent is

https://dx.doi.org/10.1021/acsnano.0c02585
ACS Nano 2020, 14, 7308–7318

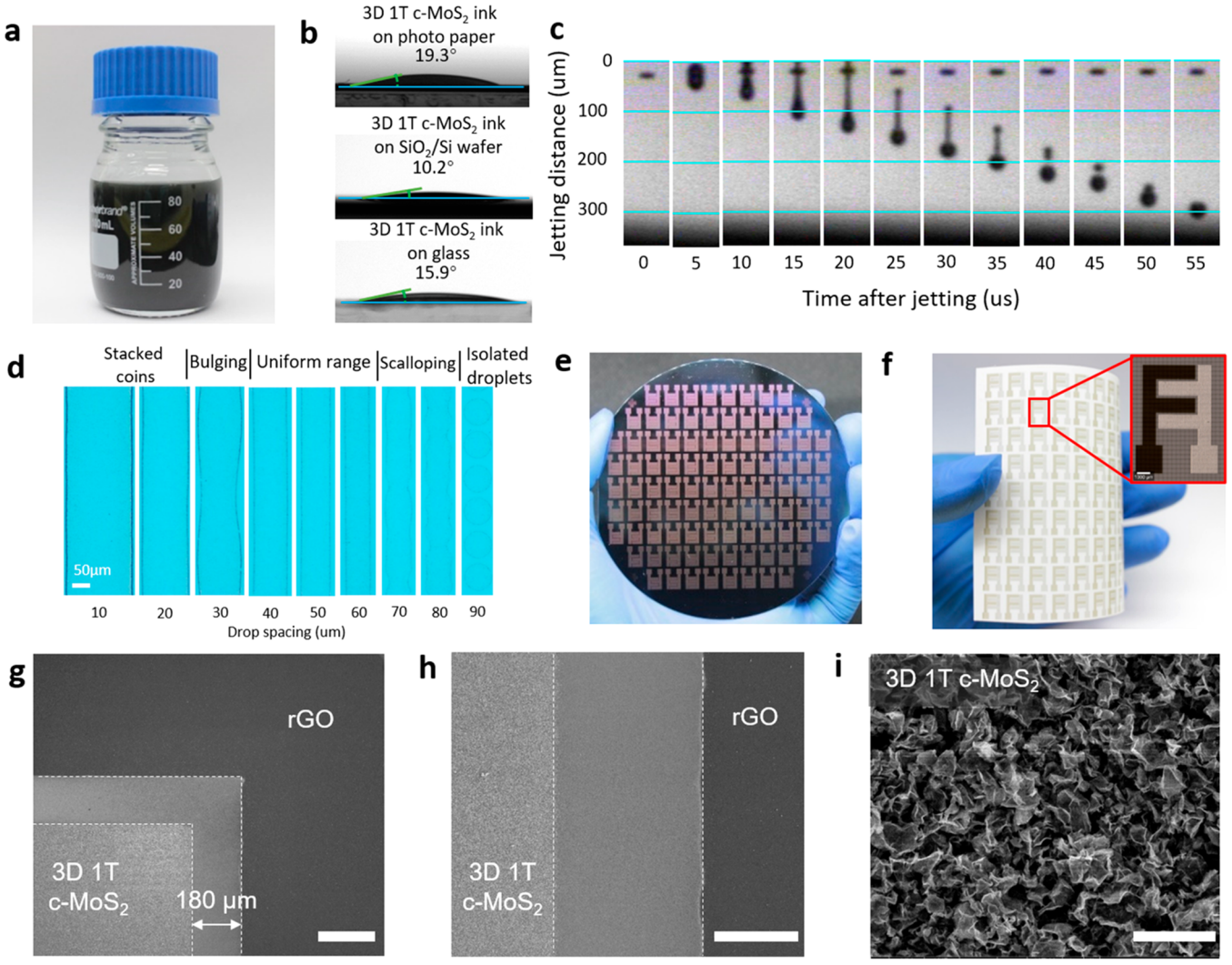

Figure 4. Inkjet printing of asymmetric micro-supercapacitors (AMSCs). (a) Prepared 100 mL of 3D 1T c-MoS_2 ink. (b) Contact angles of 3D 1T c-MoS_2 ink measured on an EPSON paper, a SiO_2/Si substrate, and a glass slide demonstrate the ability of great wetting of 3D 1T c-MoS_2 ink on a wide variety of substrates. (c) Stroboscopic images of inkjet droplets demonstrating the stable ink jetting performance. (d) 3D 1T c-MoS_2 printed on Si/SiO_2 substrates at room temperature illustrates the impact of droplet spacing on forming the line morphology. (e) 96 inkjet-printed interdigital 3D 1T c-MoS_2 MSCs on a 4 in. Si wafer. (f) 96 inkjet-printed 3D 1T c-MoS_2/rGO based AMSCs on flexible photopaper. Inset: Optical microscopic image of a single AMSC. (g, h) SEM image of a printed AMSC with well-defined borders and a straight gap of 180 μm width. (i) SEM image providing a close-up view of the dense packing of 3D 1T c-MoS_2. Scale bars: (g) 400 μm, (h) 100 μm, and (i) 1 μm, respectively.

crucial to achieving a stable dispersion and good substrate wetting. As shown in Supplementary Figure S10a, 3D 1T c-MoS_2 can be dispersed very stably in water, even after 6000 rpm centrifuging. However, the 3D 1T c-MoS_2 dispersion in water exhibited a moderate wetting capability on a majority of substrates, such as a SiO_2/Si substrate with a contact angle of 49.3° (Supplementary Figure S10e), due to the higher surface tension (γ) of DI-water (72.3 mN m^{-1}) compared with the surface energy of the targeted substrates (Si/SiO_2 or glass ~36 mJ m^{-1}, PET ~48 mJ m^{-1}, and polyimide ~44 mJ m^{-1}). After switching the dispersing medium to an IPA (surface tension ~23 mN m^{-1}) mixed 2-butanol (surface tension ~22.7 mN m^{-1}) solvent (10 vol % 2-butanol), it indeed did increase the wetting capability to a 10.2° contact angle on a SiO_2/Si substrate. It can be seen that the 3D 1T c-MoS_2 ink with the IPA and 2-butanol mixed solvent remains in a stable dispersion even after scaling up to 100 mL (Figure 4a), while the well-formulated solvent combination facilitates the universal yet enhanced wetting characteristics (Figure 4b).

To demonstrate the utility of the newly formulated 3D 1T c-MoS_2 ink, substrates, including Si/SiO_2, photopaper, glass slides, polyethylene terephthalate (PET), and polyimide films were put to the test. All substrates, regardless of their rigidity, texture, and crystallinity, demonstrated uniform wetting characteristics, as is evident by the markedly decreased contact angles (Figure 4b, Supplementary Figure S10g,h). Notable too is that 3D 1T c-MoS_2 inks took only a few seconds (7 s for photopaper, 1−3 s for PET, glass slides, and Si/SiO_2) to wet at room temperature (Supplementary Videos 1−4), leaving behind largely uniform and densely packed 3D 1T c-MoS_2.

The addition of 2-butanol also plays an important role in increasing the dispersibility. As demonstrated in Supplementary Figure S10c, 3D 1T c-MoS_2 ink still exhibited a dark color even after 6000 rpm centrifuging, which indicates significantly increased dispersibility compared to pure IPA solvent. Actually,

https://dx.doi.org/10.1021/acsnano.0c02585
ACS Nano 2020, 14, 7308−7318

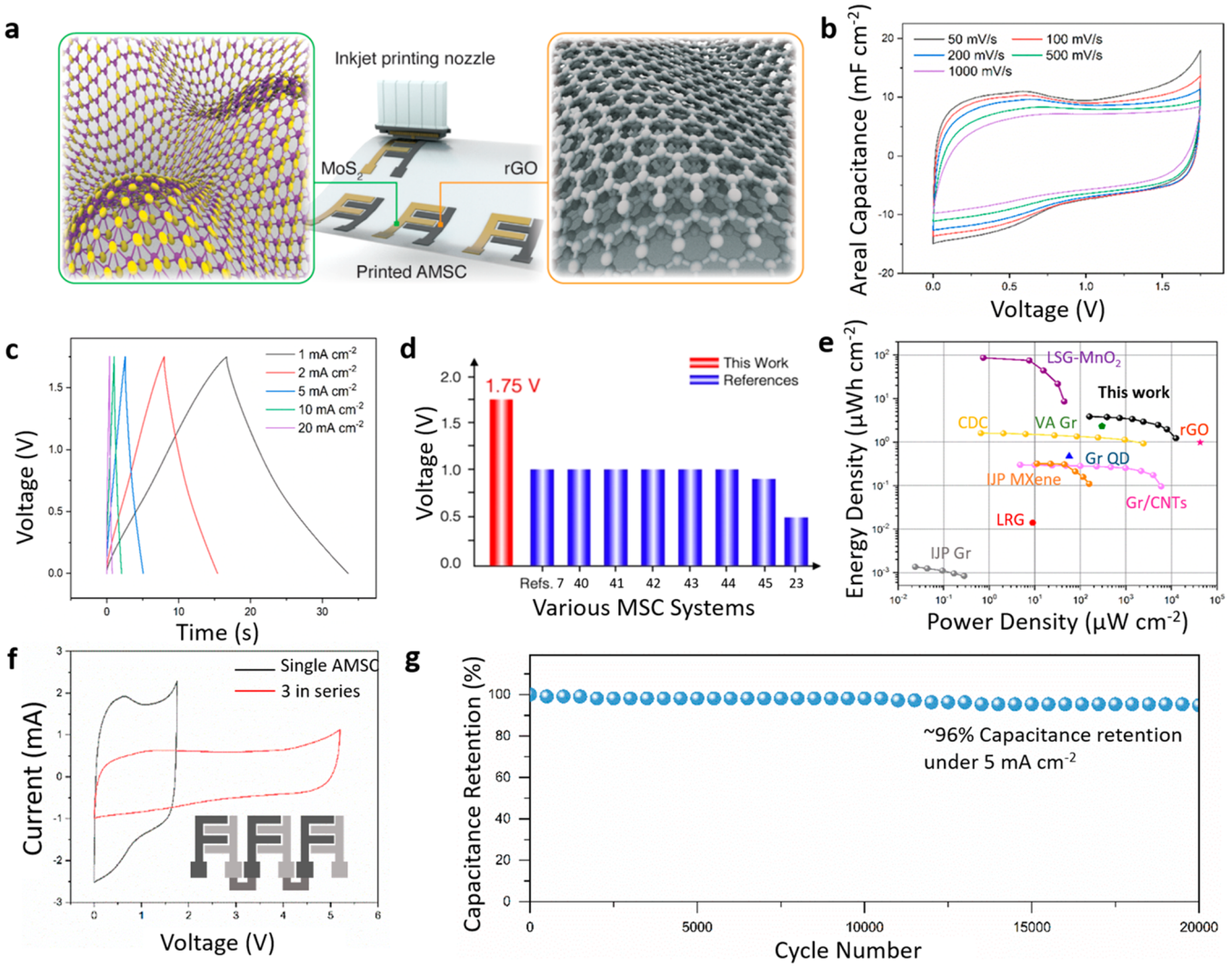

Figure 5. Electrochemical performance of inkjet-printed AMSCs. (a) Schematic depiction of the inkjet-printed asymmetric micro-supercapacitor (AMSC) comprising 3D 1T c-MoS_2 (left) and rGO (right). (b,c) CV and GCD curves of the printed AMSC in 1.0 M $MgSO_4$ aqueous electrolyte with different scan rates and current densities, respectively. (d) Output voltage of a single AMSC reaches 1.75 V, greatly surpassing previously reported printed MSC devices. The numbers indicate the references. (e) Ragone plot comparison of this work to other state-of-the-art MSC systems, including laser-reduced graphene (LRG),[40] graphene quantum dots (Gr QD),[41] graphene/carbon nanotube (Gr-CNTs) carpets,[42] thermally reduced graphene (rGO),[43] vertically aligned graphene (VA Gr),[44] inkjet-printed graphene (IJP Gr),[45] inkjet-printed MXene (IJP MXene),[23] laser-scribed graphene-MnO_2 (LSG-MnO_2),[7] and carbon-derived carbon (CDC).[6] (f) Comparison of the CV curves tested of three connected AMSCs in series with a single AMSC device. (g) Long-term cycling of the printed AMSCs readily reaches 20 000 cycles under 5 mA cm^{-2} with ~96% capacitance retention.

for the final ink formation, it only needs 2000 rpm. We attribute the fast drying and associated uniform deposition of 3D 1T c-MoS_2 inks to the low boiling points of the mixed solvent system (IPA ~82.6 °C, 2-butanol ~100 °C) in tandem with the recirculating Marangoni flow that is known to eliminate the unwanted coffee-ring effect during the printing-and-drying processes.[37,38] Supplementary Figure S10i illustrates the time-dependent contact angle variations right after printing on Si/SiO_2. Initially, the measured contact angles driven by the well-matched liquid and surface wetting characteristics continued to decrease regardless of the dispersing media. As evaporation proceeds toward the end, 3D 1T c-MoS_2 inks dispersed in DI-H_2O and IPA begin to show signs of enrichment and aggregation at the contact edges. We observed that droplets quickly contracted and left behind a series of ring-shaped patterns, thus giving rise to increased contact angles specifically at the final stage of drying. Adding a cosolvent with a higher boiling point, such as 2-butanol, is found to greatly suppress the coffee-ring effect as a result of the recirculating Marangoni flow that effectively drives 3D 1T c-MoS_2 away from the contact edges and therefore suppresses the coffee-ring effect.

In parallel, the Ohnesorge number, an index of ink jetting stability (explained in Supplementary Note 2),[21,39] was evaluated to be 10.7. This value falls well within the stable jetting range between 1 and 14. Here, the stable jetted droplets are confirmed by the collated stroboscopic images where the 3D 1T c-MoS_2 ink droplets are well directed and constantly jetted out of the nozzle even for five adjacent jetting nozzles without forming secondary droplets (Figure 4c and Supplementary Figure S11). We also observed very well-ordered printed droplet arrays on Si/SiO_2 substrates (Supplementary Figure S12a). In parallel, the drop spacing is another key parameter to determine the feature size of the printed patterns.

https://dx.doi.org/10.1021/acsnano.0c02585
ACS Nano 2020, 14, 7308−7318

As demonstrated in Figure 4d, when the drop spacing spans between 10 and 20 μm, the printed droplets overlap and then merge into a broad line pattern. When the drop spacing increases to 30 μm, the line pattern becomes bulgy due to the mixture of intermittent droplet overlapping and merging. A further increase in the drop spacing between 40 and 60 μm gives rise to straight- and narrow-line patterns. The printed line patterns develop into a scalloped outline by virtue of the insufficient droplets that are necessary to form the straight edge line when drop spacing further increases to 70 and 80 μm. When the drop spacing is beyond 90 μm, the printed line patterns veer into isolated circles. Thus, drop spacing in the range of 40−60 is the optimized parameter for inkjet printing of 3D 1T c-MoS_2 ink. Here, we inkjet printed 3D 1T c-MoS_2 ink onto various commercially available EPSON photopaper, glass slides, and Si/SiO_2 substrates without prior surface treatments (Supplementary Figure S13b−d).

The accurate deposition of active materials in the inks with well-designed patterns is a critical capability for achieving high-performance MSCs. In this project, we printed 96 AMSCs onto a rigid 4 in. Si/SiO_2 wafer or on flexible EPSON photopaper (Figure 4e,f), with rGO as the positive electrode and 3D 1T c-MoS_2 as the negative electrode. The inset to Figure 4f shows the optical microscopic image revealing the high-resolution printing of two different well-designed interdigitated electrodes. SEM images taken at selected regions of the printed 3D 1T c-MoS_2 (Figure 4i, Supplementary Figure S14a) and rGO wrinkled flakes (Supplementary Figure S15b) exhibited significantly different morphologies where densely packed 3D 1T c-MoS_2 and rGO wrinkled flakes can be clearly distinguished with well-defined straight edges and a gap of 180 μm. Raman mapping in Supplementary Figure S15 and energy-dispersive X-ray (EDX) in Supplementary Figure S16 provide additional details on the spatial distribution of individual active materials.

Figure 5a schematically demonstrates the inkjet-printing fabrication process of 3D 1T c-MoS_2//rGO interdigitated patterns. As demonstrated in the GCD curves of Figure 5c, the printed AMSC can stably charge/discharge with an output voltage of 1.75 V and shows nearly ideal triangular charge/discharge curves even at 20 mA cm^{-2}. The rate performance of the printed AMSC was evaluated with CV curves under different scan rates. This indicates 70.1% of areal capacitance retention at a high scan rate of 1000 mV s^{-1} when compared with 9.04 mF cm^{-2} at a scan rate of 20 mV s^{-1}. Combined with the largely extended stable working voltage of 1.75 V for a single device, which exceeds most previously reported MSC devices with aqueous electrolytes (Figure 5d), the single 3D 1T c-MoS_2/rGO AMSC device can achieve a high areal energy density of 3.85 μWh cm^{-2} and a maximum power density of 12.6 mW cm^{-2} (at an energy density of 1.23 μWh cm^{-2}). Figure 5e compares the energy density and power density of the printed 3D 1T c-MoS_2/rGO AMSCs with previously reported state-of-the-art MSC devices. Although the energy density alone from the 3D 1T c-MoS_2//rGO AMSCs reported in this work is still below that of the LSG-MnO_2 system,[7] it is still much better than those of the best-characterized MSCs. Note that since the energy density and power density are proportional to the square of the working voltage, the high output voltage of the printed 3D 1T c-MoS_2/rGO AMSC is in fact critical to achieving high energy storage capability. In parallel, the high working voltage is not only the key descriptor for determining the total energy density and power density but also an important parameter to drive the electrical devices through connecting in series, thus forming a "power bank" with a specific voltage to meet practical applications. Printed 3D 1T c-MoS_2/rGO AMSCs are demonstrated by connecting three devices together in series (Figure 5f). The tandem 3D 1T c-MoS_2/rGO AMSCs exhibit very good control over the operating voltage window of 5.2 V without any obvious polarization (Supplementary Figure S17a,b). Closely resembling a single 3D 1T c-MoS_2//rGO AMSC, the tandem 3D 1T c-MoS_2/rGO AMSCs can be stably charged/discharged at an output voltage of 5.2 V, while the CV curve remains largely rectangular in shape even when the scan rates are swept from 100 mV s^{-1} to 2000 mV s^{-1}. Additionally, tandem 3D 1T c-MoS_2//rGO AMSCs are found to exhibit essentially ideal triangular GCD curves along with a straight line in the EIS spectrum, again indicating the uninterrupted capacitive properties with very low internal resistance (Supplementary Figure S17c). The cycling stability is another key parameter for an MSC device. Figure 5g shows the cycling stability of the printed AMSC device, obtained from a GCD test at a current density of 5 mA cm^{-2}. The AMSC displayed ∼96% capacitance retention even after 20 000 continuous cycles.

CONCLUSIONS

In summary, high 1T ultrathin c-MoS_2 was fabricated by a scalable electrospray method and formulated into a binder-free, functional ink for scalable inkjet printing AMSC devices with a high output voltage of 1.75 V in an aqueous electrolyte. The research reported here utilizes only physical transformation of 2D exfoliated layered materials to form a 3D crumpled microstructure. The aggregation-resistant properties of the 1T 3D c-MoS_2 particles endow the electrode film with open space for electrolyte ion transport, leading to good specific capacitance and rate performance. The assembled 3D 1T c-MoS_2//rGO AMSC exhibited a wide stable working voltage of 1.75 V, excellent capacitance retention of 96% over 20 000 cycles, outstanding areal energy density of 3.85 μWh cm^{-2}, and maximum power density of 12.6 mW cm^{-2} in a $MgSO_4$ aqueous electrolyte. The formation of 3D crumpled layered materials could be a general and scalable engineering process for other emerging 2D materials, enabling the creation of functional inks with diverse functional structures. The discovery of 3D crumpled materials that maintain their ultrathin layered structure combined with scalable inkjet printing not only holds tantalizing prospects to realize better micro-supercapacitors but also has wide implications for applications beyond energy storage.

EXPERIMENTAL SECTION

Preparation of 3D 1T c-MoS_2 Solid Inks. The ce-MoS_2 sheets were prepared by a modified Li intercalation method.[30] The ce-MoS_2 aqueous dispersion was mixed with DI-H_2O and IPA in a 1:3 volume ratio before proceeding to the electrospray process. The electrospray deposition was performed using a customized setup as illustrated in Supplementary Figure S1a. In brief, the ce-MoS_2 solution (0.25 mg mL^{-1}) was fed into the spinneret (gauge 18 TW needle) by a programmable syringe pump with a flow rate of 5 μL min^{-1}. A high electric field (1.35 kV cm^{-1}) was applied through a high-voltage power supply (ES 40P-20W/DAM, Gamma High Voltage Research), and a 5 cm working distance was applied between the tip of the spinneret and the Si wafer collector. The humidity was controlled in the range of ∼40−45%. The 3D 1T c-MoS_2 powder can be conveniently collected by gently scraping the deposited powders from the collecting substrates.

https://dx.doi.org/10.1021/acsnano.0c02585
ACS Nano 2020, 14, 7308−7318

Preparation of rGO Dispersion. The rGO dispersion was prepared by the *in situ* liquid phase reduction by hydrazine.[46]

Morphological and Spectroscopic Characterization. The morphology of the 3D 1T c-MoS_2 was imaged using a field emission SEM (FE-SEM, FEI Megellan). EDX spectroscopy mapping of the spatial distribution of each element was acquired by using an EDAX detector fitted on the FE-SEM. HRTEM images were obtained on a spherical aberration coefficient (Cs)-corrected FEI Titan Cube TEM operated with an acceleration voltage of 300 kV. The high-resolution XPS measurements were carried out using a Kratos Axis Ultra DLD spectrometer equipped with a monochromatic Al K_α X-ray source ($h\nu$ = 1486.6 eV) operating at 150 W, with a multichannel plate and delay line detector under a vacuum of $\sim 10^{-9}$ mbar. The high-resolution spectra were collected within the limits of spatial resolution at a fixed analyzer pass energy of 20 eV. In order to eliminate the shifts in the HRXPS spectra associated with surface charging effects, the measurements were acquired both with and without electron beam charge compensation. For both cases, no changes were observed in the determined band alignment. The remnant binding energy shifts were referenced to the adventitious carbon (C 1s) signal. Powder X-ray diffraction patterns were recorded using a Bruker D8 Advance instrument with Cu Kα radiation (λ = 0.1542 nm) operated at 40 kV and 40 mA with a scanning speed at 2 degrees per minute. Optical spectra was taken under a WiTec alpha 300R confocal Raman microscopy system. Gratings of 1800 and 600 mesh mm^{-1} were selected with a 100× objective (NA = 0.9) from a Carl Zeiss microscope for high-resolution Raman spectra of 3D 1T c-MoS_2 and rGO, respectively. For wavelength calibration, the Si peak at 520 cm^{-1} on an undoped silicon wafer was used as the reference. Raman spatial mapping was acquired with a grating of 600 mesh mm^{-1} and a 20× objective.

Calculation and Simulation. The DFT calculations were employed to evaluate the HER overpotential within the computational hydrogen electrode model.[34] The prototypical model was constructed using 6 × 6 unit cells. The structural optimizations were performed using the revised Perdew−Burke−Ernzerhof (PRL, 1998, 80, 890) level of DFT, and electrons were described using the plane-augmented wave method[47] with an energy cutoff of 400 eV. The convergence criteria were set to be 0.001 meV per unit cell. Thereafter, the entropy part of the free energy was evaluated through vibrational frequency calculations. The electron density difference calculations were obtained by calculating the difference between the electron density of the 3D 1T c-MoS_2 with and without the adsorbed metal cations.

Electrochemical Characterization for the Stable Working Potential Ranges. The stable working potential studies of 3D 1T c-MoS_2 were carried out in different neutral cation systems. All the electrochemical measurements were performed on a Bio-Logic VMP3 potentiostat. The filtered 3D 1T c-MoS_2 dispersion mixed with 5 wt % PTFE binder was dropped onto glassy carbon as active electrode for further electrochemical measurements. The LSV for 3D 1T c-MoS_2 in different metal cation systems was carried out in a typical three-electrode system with Pt foil as a counter electrode and a saturated Ag/AgCl electrode as the reference electrode at a scan rate of 5 mV s^{-1}. All the applied potentials were converted to RHE potentials using the equation $E(vs\ \mathrm{RHE}) = E(vs\ \mathrm{Ag/AgCl}) + 0.197\ \mathrm{V} + 0.059\ \mathrm{V}*\mathrm{pH}$, after IR correction.

3D 1T c-MoS_2 Electrode Electrochemical Test for Charge Storage Capability Evaluation. The as-prepared 3D 1T c-MoS_2 filter papers were cut into 1 cm × 1 cm square pieces. The perfluoroalkoxy (PFA) T-shaped Swagelok tube fitting (PFA-820-3) served as the test body for the three-electrode measurement, graphite foil as the current collector with Pt foil as the counter electrode, and a saturated Ag/AgCl electrode as the reference electrode. For the sandwiched structure asymmetric supercapacitor test, the 3D 1T c-MoS_2 paper and rGO films were assembled as the negative electrode and the positive electrode, respectively, without adding additives, foreign stabilizers, or undergoing further treatments. Then both electrodes were tightly sealed in the test body of the PFA straight Swagelok tube fitting (PFA-820-6).

CV and GCD characterizations were carried out with a potential window of 1.0 V for both aqueous and gel electrolytes. The EIS measurements were performed at an open-circuit potential with a sinusoidal signal over a frequency range from 1 MHz to 10 mHz at an amplitude of 10 mV. The cycle life tests were conducted by GCD measurements.

The areal specific capacitance was calculated from the CV data based on eq 1:

$$C = \frac{\int i dV}{S\nu V} (\mathrm{mF\ cm^{-2}}) \tag{1}$$

where i is the discharge current in the negative CV curve, ν is the scan rate, S is the total area of the planar substrate (including the interval spaces between the interdigitated electrodes), and V represents the potential window.

The areal specific energy density and power density were calculated using eqs 2 and 3, respectively:

$$E = \frac{C\Delta V^2}{7200} (\mathrm{mWh\ cm^{-2}}) \tag{2}$$

$$P = \frac{E3600}{\Delta t} (\mathrm{mW\ cm^{-2}}) \tag{3}$$

where ΔV is the voltage drop upon discharge in the negative CV curve, Δt is the discharge time, E is the areal energy density (mWh cm^{-2}), and P is the areal power density (mW cm^{-2}).

Ink Formulation and Printing. Typically, the 3D 1T c-MoS_2 powders were dispersed into mixed solvents composed of 90 vol % IPA and 10 vol % 2-butanol and were stirred for 1 h to afford a homogeneous, stable dispersion with a concentration of 0.5 mg mL^{-1}. Next, 3D 1T c-MoS_2 inks were further sonicated with an ice bath for 1 h. The ink viscosity was characterized *via* a viscometer (Brookfield, DV3T). The surface tension and contact angles of the 3D 1T c-MoS_2 inks on different substrates were measured by a contact angle analyzer (KRUSS, EasyDrop FM40). The measurements were all conducted at room temperature (~20 °C). Meanwhile, rGO inks were prepared by diluting the rGO aqueous dispersions with a hybrid alcohol solvent to a volume ratio of 5 (H_2O):9 (IPA):1 (2-butanol). Before inkjet printing, 3D 1T c-MoS_2 and rGO inks were filtered using 1 and 5 μm syringe filters sequentially to remove unwanted sedimentations. The inkjet printer used in this work is a Fujifilm Dimatix DMP-2850, and the cartridge is a Dimatix DMC-11610 with a 10 pL droplet jetting design. The substrates, including Si/SiO_2 (SiO_2 thickness ~150 nm), glass, polyimide film, and PET, were thoroughly cleaned with acetone/ethanol/DI water prior to printing.

Inkjet Printing of AMSCs. The AMSCs were printed according to our previously reported work on rGO-based MSCs.[8] Specifically, due to the high conductivity, the printed 3D 1T c-MoS_2 and rGO interdigitated patterns directly served as both active electrodes and current collectors. The specific loading mass of 3D 1T c-MoS_2 and rGO are 0.26 and 0.34 mg cm^{-2}. Meanwhile, silver paste was painted between the square contact area followed by applying conductive copper tape to further decrease the contact resistance. The Kapton tape was used to cover the exposed copper tape to avoid any corrosion by the electrolyte especially when voltage was applied. An aqueous electrolyte of 1.0 M $MgSO_4$ was then placed on the surface and allowed to infiltrate overnight before electrochemical characterization.

ASSOCIATED CONTENT

Supporting Information

The Supporting Information is available free of charge at https://pubs.acs.org/doi/10.1021/acsnano.0c02585.

Supplementary Figures S1−17 showing the electrospray setup, physical characterization (SEM, TEM, XPS), electrochemical characterization of the MoS_2 powder and filtered MoS_2 film along with EDX mapping, Raman

https://dx.doi.org/10.1021/acsnano.0c02585
ACS Nano 2020, 14, 7308−7318

mapping, and electrochemical performance of the printed interdigital AMSC (PDF)

Supplementary video demonstrating the wetting process of 3D 1T c-MoS_2 ink on photopaper (MP4)

Supplementary video demonstrating the wetting process of 3D 1T c-MoS_2 ink on PET (MP4)

Supplementary video demonstrating the wetting process of 3D 1T c-MoS_2 ink on a glass slide (MP4)

Supplementary video demonstrating the wetting process of 3D 1T c-MoS_2 ink on a Si/SiO_2 wafer (MP4)

AUTHOR INFORMATION

Corresponding Authors

Yuanlong Shao − *College of Energy, Soochow Institute for Energy and Materials Innovations (SIEMIS), Key Laboratory of Advanced Carbon Materials and Wearable Energy Technologies of Jiangsu Province, Soochow University, Suzhou 215006, People's Republic of China; Physical Science and Engineering (PSE) Division, King Abdullah University of Science and Technology (KAUST), Thuwal 23955-6900, Saudi Arabia*; Email: ylshao@suda.edu.cn

Richard B. Kaner − *Department of Chemistry and Biochemistry, Department of Materials Science and Engineering, California NanoSystems Institute (CNSI), University of California, Los Angeles, Los Angeles, California 90095, United States*; orcid.org/0000-0003-0345-4924; Email: kaner@chem.ucla.edu

Vincent C. Tung − *Physical Science and Engineering (PSE) Division, King Abdullah University of Science and Technology (KAUST), Thuwal 23955-6900, Saudi Arabia*; Email: vincent.tung@kaust.edu.sa

Authors

Jui-Han Fu − *Physical Science and Engineering (PSE) Division, King Abdullah University of Science and Technology (KAUST), Thuwal 23955-6900, Saudi Arabia*

Zhen Cao − *Physical Science and Engineering (PSE) Division, King Abdullah University of Science and Technology (KAUST), Thuwal 23955-6900, Saudi Arabia*

Kepeng Song − *Physical Science and Engineering (PSE) Division, King Abdullah University of Science and Technology (KAUST), Thuwal 23955-6900, Saudi Arabia*

Ruofan Sun − *Physical Science and Engineering (PSE) Division, King Abdullah University of Science and Technology (KAUST), Thuwal 23955-6900, Saudi Arabia*

Yi Wan − *Physical Science and Engineering (PSE) Division, King Abdullah University of Science and Technology (KAUST), Thuwal 23955-6900, Saudi Arabia*

Atif Shamim − *Electrical Engineering Program, Computer, Electrical and Mathematical Sciences (CEMS) Division, KAUST, Thuwal 23955-6900, Saudi Arabia*

Luigi Cavallo − *Physical Science and Engineering (PSE) Division, King Abdullah University of Science and Technology (KAUST), Thuwal 23955-6900, Saudi Arabia*; orcid.org/0000-0002-1398-338X

Yu Han − *Physical Science and Engineering (PSE) Division, King Abdullah University of Science and Technology (KAUST), Thuwal 23955-6900, Saudi Arabia*; orcid.org/0000-0003-1462-1118

Complete contact information is available at: https://pubs.acs.org/10.1021/acsnano.0c02585

Notes

The authors declare no competing financial interest.

ACKNOWLEDGMENTS

V.T. gratefully acknowledges the generous support in imaging characterizations from the Molecular Foundry (User Proposal #5067), Lawrence Berkeley National Lab, supported by the Office of Basic Energy Sciences of the U.S. Department of Energy under Contract No. DE-AC02-05CH11231. V.T. and J.-H.F. are indebted to the partial support from the King Abdullah University of Science and Technology (KAUST) Office of Sponsored Research (OSR) under Award No: OSR-2018-CARF/CCF-3079. Research reported in this publication was funded by the King Abdullah University of Science and Technology (KAUST) Catalysis Center. Y.S. is indebted to the scientific illustrator, Heno Hwang at KAUST, for illustrating Figure 5a, and Shen Guang and Professor Ziping Lai for their assistance in interpretation of TEM results. R.B.K. thanks the Dr. Myung Ki Hong Endowed Chair in Materials Innovation at UCLA.

REFERENCES

(1) Kyerematen, N. A.; Brousse, T.; Pech, D. Microsupercapacitors as Miniaturized Energy-Storage Components for On-Chip Electronics. *Nat. Nanotechnol.* **2017**, *12*, 7−15.

(2) Lethien, C.; Le Bideau, J.; Brousse, T. Challenges and Prospects of 3D Micro-Supercapacitors for Powering the Internet of Things. *Energy Environ. Sci.* **2019**, *12*, 96−115.

(3) Gao, W.; Emaminejad, S.; Nyein, H. Y. Y.; Challa, S.; Chen, K.; Peck, A.; Fahad, H. M.; Ota, H.; Shiraki, H.; Kiriya, D.; Lien, D.-H.; Brooks, G. A.; Davis, R. W.; Javey, A. Fully Integrated Wearable Sensor Arrays for Multiplexed *In Situ* Perspiration Analysis. *Nature* **2016**, *529*, 509−514.

(4) Hota, M. K.; Jiang, Q.; Wang, Z.; Wang, Z. L.; Salama, K. N.; Alshareef, H. N. Integration of Electrochemical Microsupercapacitors with Thin Film Electronics for On-Chip Energy Storage. *Adv. Mater.* **2019**, *31*, 1807450.

(5) Beidaghi, M.; Gogotsi, Y. Capacitive Energy Storage in Micro-Scale Devices: Recent Advances in Design and Fabrication of Micro-Supercapacitors. *Energy Environ. Sci.* **2014**, *7*, 867−884.

(6) Huang, P.; Lethien, C.; Pinaud, S.; Brousse, K.; Laloo, R.; Turq, V.; Respaud, M.; Demortière, A.; Daffos, B.; Taberna, P. L.; Chaudret, B.; Gogotsi, Y.; Simon, P. On-Chip and Freestanding Elastic Carbon Films for Micro-Supercapacitors. *Science* **2016**, *351*, 691−695.

(7) El-Kady, M. F.; Ihns, M.; Li, M.; Hwang, J. Y.; Mousavi, M. F.; Chaney, L.; Lech, A. T.; Kaner, R. B. Engineering Three-Dimensional Hybrid Supercapacitors and Microsupercapacitors for High-Performance Integrated Energy Storage. *Proc. Natl. Acad. Sci. U. S. A.* **2015**, *112*, 4233−4238.

(8) Shao, Y.; Li, J.; Li, Y.; Wang, H.; Zhang, Q.; Kaner, R. B. Flexible Quasi-Solid-State Planar Micro-Supercapacitor Based on Cellular Graphene Films. *Mater. Horiz.* **2017**, *4*, 1145−1150.

(9) Zhang, P.; Li, Y.; Wang, G.; Wang, F.; Yang, S.; Zhu, F.; Zhuang, X.; Schmidt, O. G.; Feng, X. Zn-Ion Hybrid Micro-Supercapacitors with Ultrahigh Areal Energy Density and Long-Term Durability. *Adv. Mater.* **2019**, *31*, 1806005.

(10) Xiao, H.; Wu, Z.-S.; Chen, L.; Zhou, F.; Zheng, S.; Ren, W.; Cheng, H.-M.; Bao, X. One-Step Device Fabrication of Phosphorene and Graphene Interdigital Micro-Supercapacitors with High Energy Density. *ACS Nano* **2017**, *11*, 7284−7292.

(11) Zheng, S.; Ma, J.; Wu, Z.-S.; Zhou, F.; He, Y.-B.; Kang, F.; Cheng, H.-M.; Bao, X. All-Solid-State Flexible Planar Lithium Ion Micro-Capacitors. *Energy Environ. Sci.* **2018**, *11*, 2001−2009.

(12) Liu, Z.; Wu, Z.-S.; Yang, S.; Dong, R.; Feng, X.; Müllen, K. Ultraflexible In-Plane Micro-Supercapacitors by Direct Printing of Solution-Processable Electrochemically Exfoliated Graphene. *Adv. Mater.* **2016**, *28*, 2217−2222.

(13) Shao, Y.; El-Kady, M. F.; Sun, J.; Li, Y.; Zhang, Q.; Zhu, M.; Wang, H.; Dunn, B.; Kaner, R. B. Design and Mechanisms of Asymmetric Supercapacitors. *Chem. Rev.* **2018**, *118*, 9233−9280.
(14) McManus, D.; Vranic, S.; Withers, F.; Sanchez-Romaguera, V.; Macucci, M.; Yang, H.; Sorrentino, R.; Parvez, K.; Son, S.-K.; Iannaccone, G.; Kostarelos, K.; Fiori, G.; Casiraghi, C. Water-Based and Biocompatible 2D Crystal Inks for All-Inkjet-Printed Heterostructures. *Nat. Nanotechnol.* **2017**, *12*, 343.
(15) Hu, G.; Albrow-Owen, T.; Jin, X.; Ali, A.; Hu, Y.; Howe, R. C. T.; Shehzad, K.; Yang, Z.; Zhu, X.; Woodward, R. I.; Wu, T.-C.; Jussila, H.; Wu, J.-B.; Peng, P.; Tan, P.-H.; Sun, Z.; Kelleher, E. J. R.; Zhang, M.; Xu, Y.; Hasan, T. Black Phosphorus Ink Formulation for Inkjet Printing of Optoelectronics and Photonics. *Nat. Commun.* **2017**, *8*, 278.
(16) Kelly, A. G.; Hallam, T.; Backes, C.; Harvey, A.; Esmaeily, A. S.; Godwin, I.; Coelho, J.; Nicolosi, V.; Lauth, J.; Kulkarni, A.; Kinge, S.; Siebbeles, L. D. A.; Duesberg, G. S.; Coleman, J. N. All-Printed Thin-Film Transistors from Networks of Liquid-Exfoliated Nanosheets. *Science* **2017**, *356*, 69−73.
(17) Zhang, Y.-Z.; Wang, Y.; Cheng, T.; Yao, L.-Q.; Li, X.; Lai, W.-Y.; Huang, W. Printed Supercapacitors: Materials, Printing and Applications. *Chem. Soc. Rev.* **2019**, *48*, 3229−3264.
(18) Hu, G.; Kang, J.; Ng, L. W. T.; Zhu, X.; Howe, R. C. T.; Jones, C. G.; Hersam, M. C.; Hasan, T. Functional Inks and Printing of Two-Dimensional Materials. *Chem. Soc. Rev.* **2018**, *47*, 3265−3300.
(19) El-Kady, M. F.; Shao, Y.; Kaner, R. B. Graphene for Batteries, Supercapacitors and Beyond. *Nat. Rev. Mater.* **2016**, *1*, 16033.
(20) Shao, Y.; El-Kady, M. F.; Wang, L. J.; Zhang, Q.; Li, Y.; Wang, H.; Mousavi, M. F.; Kaner, R. B. Graphene-Based Materials for Flexible Supercapacitors. *Chem. Soc. Rev.* **2015**, *44*, 3639−3665.
(21) Torrisi, F.; Hasan, T.; Wu, W.; Sun, Z.; Lombardo, A.; Kulmala, T. S.; Hsieh, G.-W.; Jung, S.; Bonaccorso, F.; Paul, P. J.; Chu, D.; Ferrari, A. C. Inkjet-Printed Graphene Electronics. *ACS Nano* **2012**, *6*, 2992−3006.
(22) Wang, H.; Zhu, C.; Chao, D.; Yan, Q.; Fan, H. J. Nonaqueous Hybrid Lithium-Ion and Sodium-Ion Capacitors. *Adv. Mater.* **2017**, *29*, 1702093.
(23) Zhang, C.; McKeon, L.; Kremer, M. P.; Park, S.-H.; Ronan, O.; Seral-Ascaso, A.; Barwich, S.; Coileáin, C. Ó.; McEvoy, N.; Nerl, H. C.; Anasori, B.; Coleman, J. N.; Gogotsi, Y.; Nicolosi, V. Additive-Free MXene Inks and Direct Printing of Micro-Supercapacitors. *Nat. Commun.* **2019**, *10*, 1795.
(24) Acerce, M.; Voiry, D.; Chhowalla, M. Metallic 1T Phase MoS_2 Nanosheets as Supercapacitor Electrode Materials. *Nat. Nanotechnol.* **2015**, *10*, 313−318.
(25) Jiao, Y.; Hafez, A. M.; Cao, D.; Mukhopadhyay, A.; Ma, Y.; Zhu, H. Metallic MoS_2 for High Performance Energy Storage and Energy Conversion. *Small* **2018**, *14*, 1800640.
(26) Geng, X.; Zhang, Y.; Han, Y.; Li, J.; Yang, L.; Benamara, M.; Chen, L.; Zhu, H. Two-Dimensional Water-Coupled Metallic MoS_2 with Nanochannels for Ultrafast Supercapacitors. *Nano Lett.* **2017**, *17*, 1825−1832.
(27) Wu, H.; Hou, C.; Shen, G.; Liu, T.; Shao, Y.; Xiao, R.; Wang, H. MoS_2/C/C Nanofiber with Double-Layer Carbon Coating for High Cycling Stability and Rate Capability in Lithium-Ion Batteries. *Nano Res.* **2018**, *11*, 5866−5878.
(28) Li, J.; Shao, Y.; Jiang, P.; Zhang, Q.; Hou, C.; Li, Y.; Wang, H. 1T-Molybdenum Disulfide/Reduced Graphene Oxide Hybrid Fibers as High Strength Fibrous Electrodes for Wearable Energy Storage. *J. Mater. Chem. A* **2019**, *7*, 3143−3149.
(29) Chen, Y.-C.; Lu, A.-Y.; Lu, P.; Yang, X.; Jiang, C.-M.; Mariano, M.; Kaehr, B.; Lin, O.; Taylor, A.; Sharp, I. D.; Li, L.-J.; Chou, S. S.; Tung, V. Structurally Deformed MoS_2 for Electrochemically Stable, Thermally Resistant, and Highly Efficient Hydrogen Evolution Reaction. *Adv. Mater.* **2017**, *29*, 1703863.
(30) Eda, G.; Yamaguchi, H.; Voiry, D.; Fujita, T.; Chen, M.; Chhowalla, M. Photoluminescence from Chemically Exfoliated MoS_2. *Nano Lett.* **2011**, *11*, 5111−5116.
(31) Jaworek, A.; Krupa, A. Forms of the Multijet Mode of Electrohydrodynamic Spraying. *J. Aerosol Sci.* **1996**, *27*, 979−986.
(32) Ryan, C. N.; Smith, K. L.; Stark, J. P. W. Characterization of Multi-Jet Electrospray Systems. *J. Aerosol Sci.* **2012**, *51*, 35−48.
(33) Li, D.; Marquez, M.; Xia, Y. Capturing Electrified Nanodroplets under Rayleigh Instability by Coupling Electrospray with a Sol−Gel Reaction. *Chem. Phys. Lett.* **2007**, *445*, 271−275.
(34) Peterson, A. A.; Abild-Pedersen, F.; Studt, F.; Rossmeisl, J.; Nørskov, J. K. How Copper Catalyzes the Electroreduction of Carbon Dioxide into Hydrocarbon Fuels. *Energy Environ. Sci.* **2010**, *3*, 1311−1315.
(35) Huang, Y.; Nielsen, R. J.; Goddard, W. A.; Soriaga, M. P. The Reaction Mechanism with Free Energy Barriers for Electrochemical Dihydrogen Evolution on MoS_2. *J. Am. Chem. Soc.* **2015**, *137*, 6692−6698.
(36) Jaramillo, T. F.; Jørgensen, K. P.; Bonde, J.; Nielsen, J. H.; Horch, S.; Chorkendorff, I. Identification of Active Edge Sites for Electrochemical H_2 Evolution from MoS_2 Nanocatalysts. *Science* **2007**, *317*, 100−102.
(37) Lim, J. A.; Lee, W. H.; Lee, H. S.; Lee, J. H.; Park, Y. D.; Cho, K. Self-Organization of Ink-Jet-Printed Triisopropylsilylethynyl Pentacene *via* Evaporation-Induced Flows in a Drying Droplet. *Adv. Funct. Mater.* **2008**, *18*, 229−234.
(38) Hu, H.; Larson, R. G. Marangoni Effect Reverses Coffee-Ring Depositions. *J. Phys. Chem. B* **2006**, *110*, 7090−7094.
(39) Derby, B. Inkjet Printing of Functional and Structural Materials: Fluid Property Requirements, Feature Stability, and Resolution. *Annu. Rev. Mater. Res.* **2010**, *40*, 395−414.
(40) Gao, W.; Singh, N.; Song, L.; Liu, Z.; Reddy, A. L. M.; Ci, L.; Vajtai, R.; Zhang, Q.; Wei, B.; Ajayan, P. M. Direct Laser Writing of Micro-Supercapacitors on Hydrated Graphite Oxide Films. *Nat. Nanotechnol.* **2011**, *6*, 496−500.
(41) Liu, W.-W.; Feng, Y.-Q.; Yan, X.-B.; Chen, J.-T.; Xue, Q.-J. Superior Micro-Supercapacitors Based on Graphene Quantum Dots. *Adv. Funct. Mater.* **2013**, *23*, 4111−4122.
(42) Lin, J.; Zhang, C.; Yan, Z.; Zhu, Y.; Peng, Z.; Hauge, R. H.; Natelson, D.; Tour, J. M. 3-Dimensional Graphene Carbon Nanotube Carpet-Based Microsupercapacitors with High Electrochemical Performance. *Nano Lett.* **2013**, *13*, 72−78.
(43) Wu, Z. S.; Parvez, K.; Feng, X.; Müllen, K. Graphene-Based In-Plane Micro-Supercapacitors with High Power and Energy Densities. *Nat. Commun.* **2013**, *4*, 2487.
(44) Zhang, P.; Li, J.; Lv, L.; Zhao, Y.; Qu, L. Vertically Aligned Graphene Sheets Membrane for Highly Efficient Solar Thermal Generation of Clean Water. *ACS Nano* **2017**, *11*, 5087−5093.
(45) Li, L.; Secor, E. B.; Chen, K.-S.; Zhu, J.; Liu, X.; Gao, T. Z.; Seo, J.-W. T.; Zhao, Y.; Hersam, M. C. High-Performance Solid-State Supercapacitors and Microsupercapacitors Derived from Printable Graphene Inks. *Adv. Energy Mater.* **2016**, *6*, 1600909.
(46) Li, D.; Muller, M. B.; Gilje, S.; Kaner, R. B.; Wallace, G. G. Processable Aqueous Dispersions of Graphene Nanosheets. *Nat. Nanotechnol.* **2008**, *3*, 101−105.
(47) Zhang, Y.; Yang, W. Comment on "Generalized Gradient Approximation Made Simple". *Phys. Rev. Lett.* **1998**, *80*, 890.

https://dx.doi.org/10.1021/acsnano.0c02585
ACS Nano 2020, 14, 7308−7318